fractal and fractional

MDPI

Article

On the Numerical Approximation of Mobile-Immobile Advection-Dispersion Model of Fractional Order Arising from Solute Transport in Porous Media

Kamran [1], Shahzad Khan [1], Sharifah E. Alhazmi [2], Fahad M. Alotaibi [3], Massimiliano Ferrara [4,*] and Ali Ahmadian [4,5,*]

[1] Department of Mathematics, Islamia College Peshawar, Peshawar 25000, Khyber Pakhtoon Khwa, Pakistan
[2] Mathematics Department, Al-Qunfudah University College, Umm Al-Qura University, Mecca 24382, Saudi Arabia
[3] Department of Information Systems, Faculty of Computing and Information Technology (FCIT), King Abdulaziz University, Jeddah 34025, Saudi Arabia
[4] Department of Law, Economics and Human Sciences, Mediterranea University of Reggio Calabria, 89125 Reggio Calabria, Italy
[5] Department of Mathematics, Near East University TRNC, Mersin 10, Nicosia 99138, Turkey
* Correspondence: massimiliano.ferrara@unirc.it (M.F.); ahmadian.hosseini@unirc.it (A.A.)

Abstract: The fractional mobile/immobile solute transport model has applications in a wide range of phenomena such as ocean acoustic propagation and heat diffusion. The local radial basis functions (RBFs) method have been applied to many physical and engineering problems because of its simplicity in implementation and its superiority in solving different real-world problems easily. In this article, we propose an efficient local RBFs method coupled with Laplace transform (LT) for approximating the solution of fractional mobile/immobile solute transport model in the sense of Caputo derivative. In our method, first, we employ the LT which reduces the problem to an equivalent time-independent problem. The solution of the transformed problem is then approximated via the local RBF method based on multiquadric kernels. Afterward, the desired solution is represented as a contour integral in the left half complex along a smooth curve. The contour integral is then approximated via the midpoint rule. The main advantage of the LT-RBFs method is the avoiding of time discretization technique due which overcomes the time instability issues, second is its local nature which overcomes the ill-conditioning of the differentiation matrices and the sensitivity of the shape parameter, since the local RBFs method only considers the discretization points in each local domain around the collocation point. Due to this, sparse and well-conditioned differentiation matrices are produced, and third is the low computational cost. The convergence and stability of the numerical scheme are discussed. Some test problems are performed in one and two dimensions to validate our numerical scheme. To check the efficiency, accuracy, and efficacy of the scheme the 2D problems are solved in complex domains. The numerical results confirm the stability and efficiency of the method.

Keywords: solute transport model; local RBFs method; Laplace transform; contour integration method; Talbot's contour; mid point rule

Citation: Kamran; Khan, S.; Alhazmi, S.E.; Alotaibi, F.M.; Ferrara, M.; Ahmadian, A. On the Numerical Approximation of Mobile-Immobile Advection-Dispersion Model of Fractional Order Arising from Solute Transport in Porous Media. *Fractal Fract.* **2022**, *6*, 445. https://doi.org/10.3390/fractalfract6080445

Academic Editor: Zine El Abiddine Fellah

Received: 4 July 2022
Accepted: 12 August 2022
Published: 17 August 2022

1. Introduction

In groundwater, streams, and rivers, the transportation of solutes is affected by physical characteristics or the heterogeneity of different regions. For a long time, solute transportation has been a hot topic in theory and experimental study. In the recent past, the mobile/immobile (MI) model has been successfully used. It should be emphasized that the transportation model can describe the connectivity and heterogeneity of spatial characteristics in a better way to transport solutes in the general network. MI method has been widely praised by hydrologists who study water transport in unsaturated and saturated regions [1].

The advection-dispersion equation (ADE) characterizes the transport of solutes in porous media. However, according to reports, the ADE model faces problems in interpreting the transport process in fractured, homogeneous, and even heterogeneous media. In [2], research shows that the MI model is better than ADE in both fractured and porous media. More details can be found in [1,3–6]. Fractional differential equations have become very useful to model numerous phenomena in different areas such as economics, chemistry, physics, acoustics, biology, viscoelasticity, engineering, and electromagnetics [6–13]. It is worth to mention that the main aspect of arbitrary order derivative is the the memory effect, i.e., the future state of a physical system depends on the present as well as past states. It is natural to use fractional derivatives while modeling physical or dynamical systems in various applications such as viscoelastic materials, frequency-dependent damping behavior of materials, and motion of a large thin plate in a Newtonian fluid, etc.

The fractional mobile-immobile advection-dispersion equation is achieved by replacement of first order derivative with fractional derivative in classical mobile-immobile advection-dispersion equation [13]. Here we consider a fractional MI model of the form

$$\beta_1 D_t u(\bar{\xi},t) + \beta_2 D_t^{\alpha} u(\bar{\xi},t) - \mathcal{L}u(\bar{\xi},t) = S(\bar{\xi},t),\ \bar{\xi} \in \Omega,\ 0 \le t \le T. \tag{1}$$

subject to the initial-boundary conditions

$$u(\bar{\xi},0) = u_0,\ \bar{\xi} \in \Omega, \tag{2}$$

and

$$\mathcal{L}_{\mathcal{B}} u(\bar{\xi},t) = Q(\bar{\xi},t),\ \bar{\xi} \in tial\Omega, \tag{3}$$

where $u(\bar{\xi},t)$ represents the solute concentration, $S(\bar{\xi},t)$ is the source term, β_1, β_2 are constants, t and $\bar{\xi} = (\xi,\zeta)$ are the time and space variables respectively. u_0, $Q(\bar{\xi},t)$ are given functions of t and $\bar{\xi}$. Ω is the domain and $tial\Omega$ is its boundary. $\mathcal{L}$ is the linear differential operator and $\mathcal{L}_{\mathcal{B}}$ is the boundary differential operator and ${}_0^c D_t^{\alpha} u(\bar{\xi},t)$ is the Caputo derivative of $u(\bar{\xi},t)$ of fractional order $\alpha \in (0,1)$ which is defined as

$${}_0^c D_t^{\alpha} u(\bar{\xi},t) = \frac{1}{\Gamma(1-\alpha)} \int_0^t \frac{D_s u(\bar{\xi},s)}{(t-s)^{\alpha}} ds.$$

If $u(\bar{\xi},t)$ is a piecewise continues function defined on $(0,\infty)$, and is of exponential order, then its Laplace transform (LT) is

$$\widehat{u}(\bar{\xi},z) = \mathscr{L}\{u(\bar{\xi},t)\} = \int_0^{\infty} e^{-zt} u(\bar{\xi},t) dt,\ t > 0.$$

The LT of ${}_0^c D_t^{\alpha} u(\bar{\xi},t)$ is given as

$$\mathscr{L}\{{}_0^c D_t^{\alpha} u(\bar{\xi},t)\} = z^{\alpha}\widehat{u}(\bar{\xi},z) - \sum_{i=0}^{m-1} z^{\alpha-i-1} u^{(i)}(\bar{\xi},0).$$

For the stability and convergence of the fraction MI model defined in Equations (1) and (3) the readers are referred to [14]. For existence of the fractional MI model the readers are referred to [13]. The solution of such type of problem has been considered by many researchers for example in [15] the authors proposed an implicit finite difference method for the numerical approximation of the MI model of fractional order. The authors in [16] have proposed an implicit numerical method for a class of MI advection-dispersion models of space-time fractional orders. In [17] the Jacobi spectral collocation method is developed for the time variable order MI model. Similarly the authors in [18] developed a numerical method based on second-kind shifted Chebyshev polynomials and finite difference method for the numerical treatment of MI models. In [19], the authors have studied the numerical solution of the time-fractional MI transport equation using the finite element method.

The authors in [20] have used the physical nonequilibrium model to describe the transport of solutes in porous media. They have used the finite volume method for investigating the numerical solution of the physical nonequilibrium model. Sharma et al. [21] studied the behavior of solute transport through MI soil column based on the laboratory study. Gao et al. [22], in their study, have analyzed the behavior of solute transport in convection-dispersion transport model as compared to homogeneous and heterogeneous porous media. Other robust methods for solving the MI model can be found in [6,23,24] and there references. The finite volume method, finite element method, and finite difference method are all mesh-based methods and have powerful features, but in these methods the need to create a polygonization, either in the domain or on its boundary is a common drawback. Mesh generation is the most time-consuming part of the solution process and for complex geometries, problems can occur with implementation.

However, in recent years great attention was given to the meshless methods which operate with nodes rather than meshes. The attractive features of meshless methods are (i) they do not require grid generation which can be a difficult task in three-dimensional cases; (ii) they are more appropriate than mesh-based methods in the cases of large deformation or moving discontinuities. One of the common characteristics of all meshless methods is their ability to construct functional interpolation or approximation entirely from information at a set of scattered nodes, among which there is no pre-specified connectivity or relationships. A large number of meshless methods have been proposed to date. The element-free Galerkin method [25], the boundary particle method [26], the partition of unity method [27] are among popular meshless methods.

Another group of meshless methods, which are based on radial basis functions (RBFs), are one of the best tools for approximating the solution of different real-world problems [12,28]. The main features of RBFs are their smoothness, spectral convergence, and ease of implementation. Meshless methods based RBFs are global radial basis functions methods (GRBFM) [29], and local radial basis functions methods (LRBFM) [30]. The main drawback of GRBFM is that it involves full system matrices that result from the discretization of the PDEs. These system matrices are often ill-conditioned and extremely sensitive to the selection of the shape parameters in RBFs. The accuracy of the approximation and the conditioning of the system matrix depends on the value of the shape parameter. In general, for a fixed number of centers N, more accurate approximations are produced for small value of shape parameters, but also produce an ill-conditioned system matrix. The condition number of the system matrix varies with N for the fixed shape parameter. In practice, the value of the shape parameter must be adjusted with N in order to produce a well-conditioned system matrix. For selecting good values of the shape parameter many attempts have been made [31–33]. For GRBFM, selecting a good value of shape parameter is still an open question. The main idea of LRBFM is that it uses a small subset of available centers instead of the whole domain which reduces the size of the system matrix at the expense of solving many small-size matrices. The size of each small matrix is the same as the number of nodes in the subdomain of influence of each center. LRBFM was first time introduced in [34] for diffusion problems. One of the important benefits of the LRBFM is that the multiquadrics (MQ) or inverse multiquadrics (IMQ) shape parameter affects the results slightly [35]. Due to handiness LRBFM has been applied to many complex phenomena [11,36–38] and their references. The main drawback of the LRBFM is that this method does not work for elliptic problems in a straight forward way. Also since all these methods are based on finite difference time stepping techniques. The drawback of time stepping technique is that it does not always lead to a stable solution. A finite difference scheme is stable if the errors made at one timestep do not cause the errors to be enlarged as the calculations are continued. A finite difference time stepping scheme is stable if the errors remain constant or decay during computations. Also, in time-stepping techniques, the accuracy is achieved at a very small step size, and hence this method encounter an exponential increase of computing costs with advancing time and thus have low efficiency in the simulation of long time history fractional problems [39–41]. In order to circumvent

the drawback of the finite difference time stepping method an alternative way is to use LT in time. In literature the LT in conjunction with other methods has been used by many authors. In [40] the authors coupled LT with the boundary element method. The authors in [41] used LT in conjunction with the boundary particle method for the numerical approximation of time-fractional diffusion equations. In [42] the authors for the first time used LT combined with the boundary integral equation method. In [43] the author coupled LT with finite element method for parabolic type differential equations. The coupling of LT with other methods can be found in the references [44–46]. In this article we propose a local RBF-based method coupled with LT for the numerical solution of solute transport models.

2. Proposed Method

In our numerical scheme for approximating the solution of the problem defined (1) and (3), first we employ the Laplace transform to reduce the given problem to an equivalent elliptic problem as follows

$$\beta_1[z\widehat{u}(\bar{\xi},z)-u_0]+\beta_2[z^{\alpha}\widehat{u}(\bar{\xi},z)-z^{\alpha-1}u_0]-\mathcal{L}\widehat{u}(\bar{\xi},z)=\widehat{S}(\bar{\xi},z), \tag{4}$$

$$\mathcal{L}_{\mathcal{B}}\widehat{u}(\bar{\xi},z)=\widehat{Q}(\bar{\xi},z), \tag{5}$$

which is simplified as

$$[(\beta_1 z+\beta_2 z^{\alpha})I-\mathcal{L}]\widehat{u}(\bar{\xi},z)=\widehat{h}_1(\bar{\xi},z), \tag{6}$$

$$\mathcal{L}_{\mathcal{B}}\widehat{u}(\bar{\xi},z)=\widehat{Q}(\bar{\xi},z), \tag{7}$$

where

$$\widehat{h}_1(\bar{\xi},z)=\beta 1u_0+\beta_2 z^{\alpha-1}u_0+\widehat{S}(\bar{\xi},z).$$

Now we need to solve the system of equations defined (6) and (7) in parallel for each quadrature node z in the LT space. For this we discretize the linear differential operator $\mathcal{L}$ and boundary operator $\mathcal{L}_{\mathcal{B}}$ using the local RBF method. In the final step we obtain the solution of our problem (1) and (2) as a Bromwich integral. In the next section we describe the local RBF method.

2.1. Local RBF Method

In this section, we propose a local RBF method for approximating the solution of the elliptic problem defined in (6) and (7) in LT space. For a given set of nodal points $\{\bar{\xi}_i\}_{i=1}^{N}\in\Omega$, where $\Omega\subset\mathbb{R}^m$, $m\geq 1$. The approximation of $\widehat{u}(\bar{\xi})$ via local RBF method can be obtained as

$$\widehat{u}(\bar{\xi}_i)=\sum_{\bar{\xi}_h\in\Omega_i}\lambda_h^i\phi(\|\bar{\xi}_i-\bar{\xi}_h\|), \tag{8}$$

where the function $\phi(r)$ is a radial kernel, and r is the distance from the node $\bar{\xi}_i$ to the node $\bar{\xi}_h$, $\lambda^i=\{\lambda_h^i\}_{h=1}^{n}$ is the vector of unknown coefficients which can be obtained using interpolation conditions. The set Ω_i is the subdomain containing the node $\bar{\xi}_i$, and its n neighboring nodes around it. Thus we obtain N small size $n\times n$ linear systems as follows

$$\widehat{u}^i=\Phi^i\lambda^i, i=1,2,\ldots,N, \tag{9}$$

where Φ^i is the interpolation matrix with entries $b_{lj}^i=\phi(\|\bar{\xi}_l-\bar{\xi}_h\|)$, where $\bar{\xi}_l,\bar{\xi}_h\in\Omega_i$, the unknowns $\lambda^i=\{\lambda_h^i\}_{h=1}^{n}$ are obtained by solving each small size $n\times n$ system. Similarly the operator $\mathcal{L}$, can be approximated as

$$\mathcal{L}\widehat{u}(\bar{\xi}_i)=\sum_{\bar{\xi}_h\in\Omega_i}\lambda_h^i\mathcal{L}\phi(\|\bar{\xi}_i-\bar{\xi}_h\|), \tag{10}$$

the above Equation (10) can be expressed as

$$\mathcal{L}\widehat{u}(\bar{\xi}_i) = \lambda^i \cdot \nu^i, \tag{11}$$

where ν^i is a n-row vector and λ^i is a n-column vector with entries shown below

$$\nu^i = \mathcal{L}\phi(\|\bar{\xi}_i - \bar{\xi}_h\|),\ \bar{\xi}_h \in \Omega_i, \tag{12}$$

solving Equation (9) for λ^i we have,

$$\lambda^i = (\Phi^i)^{-1}\widehat{u}^i, \tag{13}$$

From Equation (13) we use λ^i in Equation (11),

$$\mathcal{L}\widehat{u}(\bar{\xi}_i) = \nu^i(\Phi^i)^{-1}\widehat{u}^i = \mathbf{w}^i\widehat{u}^i \tag{14}$$

where,

$$\mathbf{w}^i = \nu^i(\Phi^i)^{-1}, \tag{15}$$

thus we have

$$\mathcal{L}\widehat{u} \equiv \mathbf{D}\widehat{u}, \tag{16}$$

The matrix $\mathbf{D}_{N\times N}$ is the local meshless approximate for $\mathcal{L}$ at each node $\bar{\xi}_i$. The same procedure can be adapted for the boundary operator $\mathcal{L}_\mathcal{B}$.

2.2. Selecting Optimal Shape Parameter

In literature a large number of radial kernels are available. In this paper we have selected the multiquadrics (MQ) radial kernel defined by $\phi(r,\varepsilon) = \sqrt{1+r^2\varepsilon^2}$. The MQ kernel contains the shape parameter ε. Accurate results can be achieved by varying the value of ε. To quantify the sensitivity to perturbation of the linear system and to estimate the accuracy of approximate solution the condition number κ of the system matrix Φ^i is used. In this work we have used utilized the uncertainty principle [47] for obtaining the optimal value of ε. In RBFs methods, better accuracy is achieved for ill-conditioned system matrices. Using this technique smallest error occurs when κ satisfies $10^{12} < \kappa < 10^{16}$. We express the system matrix Φ^i as $\mathbf{E}, \mathbf{D}, \mathbf{S} = svd(\Phi^i)$. Where $\mathbf{E}_{n\times n}$, $\mathbf{V}_{n\times n}$ are $n \times n$ orthogonal matrices, and $\mathbf{S}_{n\times n}$ is the $n \times n$ diagonal matrix containing singular values of the system matric Φ^i. Hence the matrix condition number is calculated as $\kappa = \|\Phi^i\|\|(\Phi^i)^{-1}\| = \max(\mathbf{D})/\min(\mathbf{D})$.

The following algorithm in MATLAB can be used to for optimizing the shape parameter [30].

Step i: set $\kappa = 1$
Step ii: select $10^{12} < \kappa < 10^{16}$
Step iii: while $\kappa > \kappa_{maximum}$ and $\kappa < \kappa_{minimum}$
Step iv: $\mathbf{E}, \mathbf{D}, \mathbf{S} = svd(\Phi^i)$
Step v: $\kappa = \dfrac{\max(\mathbf{D})}{\min(\mathbf{D})}$
Step vi: if $\kappa < \kappa_{minimum}$, $\varepsilon = \varepsilon - \varepsilon Increament$
Step vii: *else* $\kappa > \kappa_{maximum}$, $\varepsilon = \varepsilon + \varepsilon Increament$
return ε.

When we get the optimal value of shape parameter ε, we use svd to compute $(\Phi^i)^{-1} = (\mathbf{EDS^T})^{-1} = \mathbf{SD^{-1}E^T}$ (see [48]). Hence the weights $\mathbf{w}^i$ in (15) can be computed.

2.3. Numerical Inverse Laplace Transform

After the approximation of the spatial operators $\mathcal{L}$ and $\mathcal{L}_\mathcal{B}$ using the local RBF method the system (6) and (7) is solved in parallel for each point z. Afterwards we implement the inverse Laplace transform to convert the local RBF solutions from Laplace space to the time

domain. Here we employ the contour integration method. We obtain the solution as a Bromwich integral defined below [49]

$$u(\bar{\xi},t)=\frac{1}{2\pi i}\int_{\rho-i\infty}^{\rho+i\infty}exp(zt)\widehat{u}(\bar{\xi},z)dz=\frac{1}{2\pi i}\int_{\Gamma}exp(zt)\widehat{u}(\bar{\xi},z)dz,\ \rho>\rho_0, \tag{17}$$

where Γ is a suitable chosen path joining $\rho-i\infty$ to $\rho+i\infty$. In order to obtain the solution of the problem defined in (1) and (3), we need to solve the integral defined in Equation (17). In many situations, solving Equation (17) may be difficult analytically, so the best way is to use numerical methods. Numerical approximation of the integral defined in Equation (17) is hard to obtain because of the slowly decaying transform $\widehat{u}(\bar{\xi},z)$, $z=\rho+y$, $|y|\to\infty$ and highly oscillatory exponential factor on the contour of integration Γ. To handle the slow decay of the transformed function $\widehat{u}(\bar{\xi},z)$. In [50] Talbot suggested that the Bromwich line $z=\rho+y$, $-\infty<y<\infty$ be transformed to a contour whose real part begins at negative infinity in the third quadrant, and terminates with the real part again going to negative infinity in the second quadrant. In such a case the integrand in Equation (17) will decay rapidly because of the exponential factor, and this makes the integral defined by Equation (17) suitable for approximation by trapezoidal or midpoint rule [51]. By Cauchy's theorem such a deformation is allowed if $\widehat{u}(\bar{\xi},z)$ has no singularities, and $\widehat{u}(\bar{\xi},z)\to 0$ if $Re(z)\leq\rho_0$ as $|z|\to\infty$. (If $\widehat{u}(\bar{\xi},z)$ have singularities with unbounded imaginary part, then Talbot method may not work). In this work, we utilized Talbot's contour defined as [52]

$$\Gamma: z=z(v)=\frac{M}{t}\{-\sigma+\mu v\cot(\gamma v)+\nu\iota v\},\ -\pi\leq v\leq\pi, \tag{18}$$

where $Rez(\pm\pi)=-\infty$, and the values of the parameters $\nu,\ \sigma,\ \gamma,\ \mu$, be specified by the user. From Equations (17) and (18), we get

$$u(\bar{\xi},t)=\frac{1}{2\pi i}\int_{-\pi}^{\pi}exp(z(v)t)\widehat{u}(\bar{\xi},z(v))z'(v)dv. \tag{19}$$

In order to approximate Equation (19), we use the mid-point rule with step $k=\frac{2\pi}{M}$, as

$$\begin{aligned}u_k(\bar{\xi},t)&=\frac{1}{Mi}\sum_{j=1}^{M}e^{z_jt}\widehat{u}(\bar{\xi},z_j)\acute{z}_j,\\ \text{for } v_j&=-\pi+(j-\frac{1}{2})k,\ \ z_j=z(v_j),\ z_j'=z'(v_j).\end{aligned} \tag{20}$$

2.4. Accuracy and Convergence of the Method

In our approximation process via our proposed method. First, we utilized the Laplace transform to remove the time variable. The transformation of the time-dependent problem to an equivalent elliptic problem via Laplace transform incurs no errors. Next, we use the RBF method in local form for approximating the elliptic PDE. The localized meshless has error estimate of order $O(\zeta^{\frac{1}{\epsilon h}})$, $0<\zeta<1$, where h is the fill distance and ϵ is the shape parameter [28]. Finally, we obtain our solution as an integral in Equation (19), while approximating this integral using some suitable quadrature rule, the convergence is achieved at different rates depending on Γ. The convergence order of quadrature rule relays on the temporal domain $[t_0,T]$ and the step k. For best accuracy one needs the best contour of integration. For this purpose a large number of contours have been proposed in the literature. In our work we utilize the recently proposed contour known as improved Talbot contour [52] with best values of the parameters as given below

$$\mu=0.50170,\ \sigma=0.61220,\ \gamma=0.64070,\ \text{and}\ \nu=0.26450,$$

with error estimate as

$$\mathrm{E} = |u(\bar{\xi}, t) - u_k(\bar{\xi}, t)| = O(e^{-1.358M}).$$

3. Stability

To discuss the stability of our numerical scheme, we write the systems defined in (6) and (7) in discrete form as given below

$$\mathrm{T}\widehat{u} = \mathbf{b}, \tag{21}$$

here the matrix T is a sparse differentiation matrix. The stability constant for the system in (21) is defined as

$$\mathrm{Q} = \sup_{\widehat{u}\neq 0} \frac{\|\widehat{u}\|}{\|\mathrm{T}\widehat{u}\|}, \tag{22}$$

the constant Q is finite for any norm $\|.\|$ on R^N. From (22), we have

$$\|\mathrm{T}\|^{-1} \leq \frac{\|\widehat{u}\|}{\|\mathrm{T}\widehat{u}\|} \leq \mathrm{Q}, \tag{23}$$

Also for the pseudoinverse $\mathrm{T}^{\dagger}$ of T, we can write

$$\|\mathrm{T}^{\dagger}\| = \sup_{\mu\neq 0} \frac{\|\mathrm{T}^{\dagger}\mu\|}{\|\mu\|}. \tag{24}$$

Hence

$$\|\mathrm{T}^{\dagger}\| \geq \sup_{\mu=\mathrm{T}\widehat{u}\neq 0} \frac{\|\mathrm{T}^{\dagger}\mathrm{T}\widehat{u}\|}{\|\mathrm{T}\widehat{u}\|} = \sup_{\widehat{u}\neq 0} \frac{\|\widehat{u}\|}{\|\mathrm{T}\widehat{u}\|} = \mathrm{Q}. \tag{25}$$

Equations (23) and (25) confirms the bounds for the constant Q. Calculation of the pseudoinverse for (21) may be hard numerically, but it guarantees stability. The MATLAB's function condest can be used to estimate $\|\mathrm{T}^{-1}\|_{\infty}$ for square matrices, thus we have

$$\mathrm{Q} = \frac{condest(\mathrm{T}')}{\|\mathrm{T}\|_{\infty}} \tag{26}$$

4. Numerical Experiments

To verify the efficiency of our proposed numerical method we have considered different models. We performed our experiments in MATLAB R2019a on a Windows 10 (64 bit) PC equipped with an Intel(R) Core(TM) i5-3317U CPU @ 1.70 GHz and with 4 GB of RAM. To validate the theoretical results we use the absolute error L_{abs}, and the maximum absolute error L_{∞} defined as

$$L_{abs} = |u(\bar{\xi}_i, t) - u_k(\bar{\xi}_i, t)|$$

$$L_{\infty} = \|u(\bar{\xi}_i, t) - u_k(\bar{\xi}_i, t)\|_{\infty} = \max_{1\leq i\leq N}(|u(\bar{\xi}_i, t) - u_k(\bar{\xi}_i, t)|).$$

4.1. Problem 1

In the first test, we consider a mobile-immobile advection-dispersion equation of fractional order as [6]

$$D_t u(\xi, t) + D_t^{\alpha} u(\xi, t) = D_{\xi\xi} u(\xi, t) - D_{\xi} u(\xi, t) + f(\xi, t),\ \xi \in [0, 1],\ t > 0,$$

where

$$f(\xi, t) = exp\left(\frac{-(\xi - 0.5)^2}{\gamma}\right)\left[\frac{1}{\Gamma(2-\alpha)} t^{1-\alpha} + 1 + \frac{2t}{\gamma}\left(1 - (\xi - 0.5) - \frac{2}{\gamma}(\xi - 0.5)\right)\right],$$

the analytic solution is

$$u(\xi,t) = t\,exp\left(\frac{-(\xi-0.50)^2}{\gamma}\right).$$

$u(\xi,t)$ is a Gaussian distribution centered at $\xi = 0.5$ with height t and γ is the standard deviation. The problem is solved using the proposed method the boundary and initial data are extracted from the analytic solution. Table 1 shows the results for fractional orders $\alpha = 0.4,\ 0.9$ and various spatial nodes N in the global, and n local domains and quadrature nodes M. The CPU time, the condition number (κ) of the differentiation matrix, the shape parameter (ε) are also shown in Table 1. From Table 1, we observe that the proposed numerical scheme produced results with good accuracy. We have compared our results with another RBF method, it can be seen that our results are better. The profiles of approximate and analytic solution with $\gamma = 0.1, \alpha = 0.8, N = 95, M = 24$, and $n = 10$, at $t = 1$ are depicted in Figure 1a, and the plot of absolute error in Figure 1b. In Figure 2a the profiles of exact and analytic solutions with $\gamma = 0.001, \alpha = 0.8, N = 95, M = 24$, and $n = 10$, at $t = 1$ are shown, and the plot of absolute error in Figure 2b. We see that the method has produced good results for $\gamma = 0.001$. The problem has a sharp Gaussian pulse when $\gamma = 0.001$. The contour plot of absolute error with $N = 60, n = 10, \alpha = 0.5, M = 26$, and $\gamma = 0.01$ is depicted in Figure 3. The surface plots of the approximate and analytic solutions of problem 1 are presented in Figure 4a,b respectively. All the results depicted in the figures and Table 1 demonstrate that the numerical results agree well with the exact solution. From the results, we conclude that the proposed method is stable and accurate.

Table 1. The approximate solutions with $\gamma = 0.1$, $\xi \in [0,1]$, and $t = 1$, corresponding to Problem 1.

N	n	M	ε	κ	$\alpha = 0.4$		$\alpha = 0.9$	
					L_∞	$CPU(s)$	L_∞	$CPU(s)$
20	5	24	0.5	1.53×10^{12}	5.46×10^{-4}	0.089142	5.55×10^{-4}	0.089602
30			0.8	1.05×10^{12}	5.98×10^{-5}	0.194214	5.93×10^{-5}	0.110046
50			1.3	1.43×10^{12}	1.41×10^{-5}	0.133385	1.40×10^{-5}	0.141561
60			1.6	1.20×10^{12}	2.84×10^{-5}	0.118387	5.13×10^{-5}	0.105559
70			1.9	1.06×10^{12}	1.66×10^{-5}	0.122090	1.46×10^{-5}	0.109360
80			2.1	1.41×10^{12}	6.72×10^{-6}	0.110556	9.10×10^{-6}	0.108059
100			2.7	1.15×10^{12}	9.11×10^{-6}	0.132338	9.11×10^{-6}	0.131337
75	5	26	2.0	1.23×10^{12}	2.94×10^{-5}	0.108321	2.92×10^{-5}	0.108939
	7		4.5	1.08×10^{12}	2.99×10^{-5}	0.111992	2.96×10^{-5}	0.108220
	8		5.5	1.05×10^{12}	5.11×10^{-5}	0.112198	5.05×10^{-5}	0.107458
	9		6.2	1.21×10^{12}	7.79×10^{-5}	0.117348	7.70×10^{-5}	0.123790
	10		6.9	1.06×10^{12}	8.26×10^{-5}	0.113088	8.16×10^{-5}	0.120238
	12		7.8	1.09×10^{12}	7.12×10^{-5}	0.141167	7.06×10^{-5}	0.386028
[6]					4.07×10^{-4}		4.56×10^{-4}	

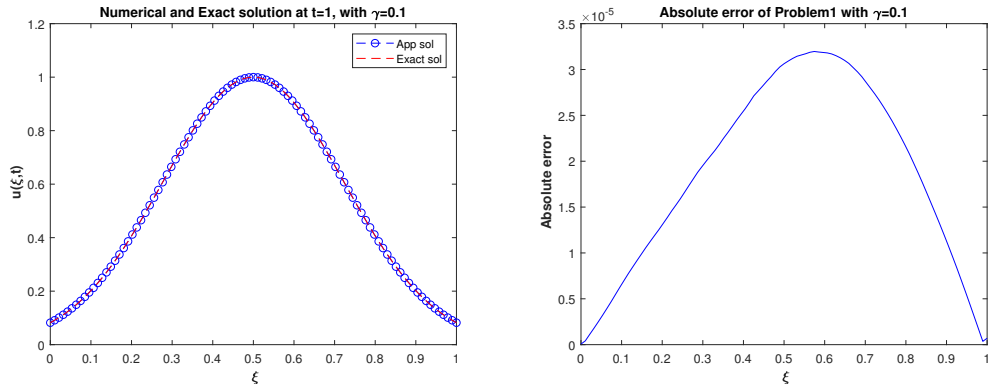

(**a**) (**b**)

Figure 1. (**a**) The approximate and analytic solutions of Problem 1 with $\gamma = 0.1, \alpha = 0.8, N = 95, M = 24$, and $n = 10$, at $t = 1$. (**b**) Plot of absolute error of Problem 1 with $\gamma = 0.1, \alpha = 0.8, N = 95, M = 24$, and $n = 10$, at $t = 1$.

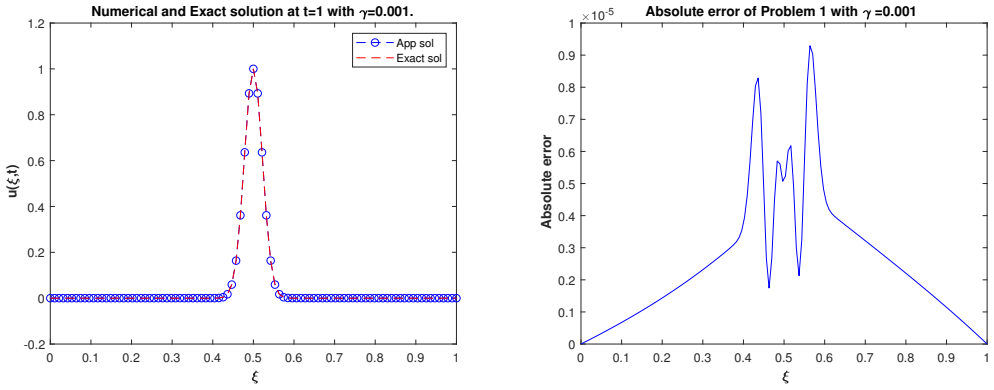

(**a**) (**b**)

Figure 2. (**a**) The approximate and analytic solutions of Problem 1 with $\gamma = 0.001, \alpha = 0.8, N = 95$, $M = 24$, and $n = 10$, at $t = 1$. We see that the problem has sharp Gaussian pulse when $\gamma = 0.001$. (**b**) Plot of absolute error of Problem 1 with $\gamma = 0.001, \alpha = 0.6, N = 150, M = 28$, and $n = 7$, at $t = 1$.

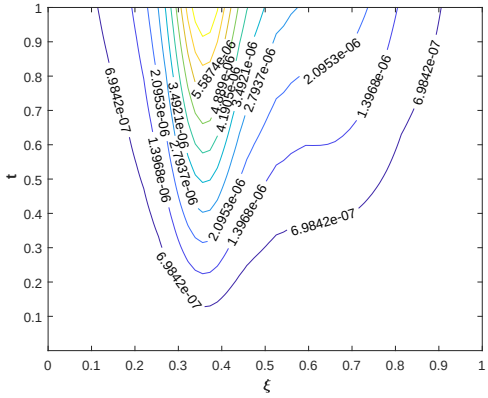

Figure 3. Contour plot of the absolute error of Problem 1 with $N = 60, n = 10, M = 26,\ \alpha = 0.5$, and $\gamma = 0.01$.

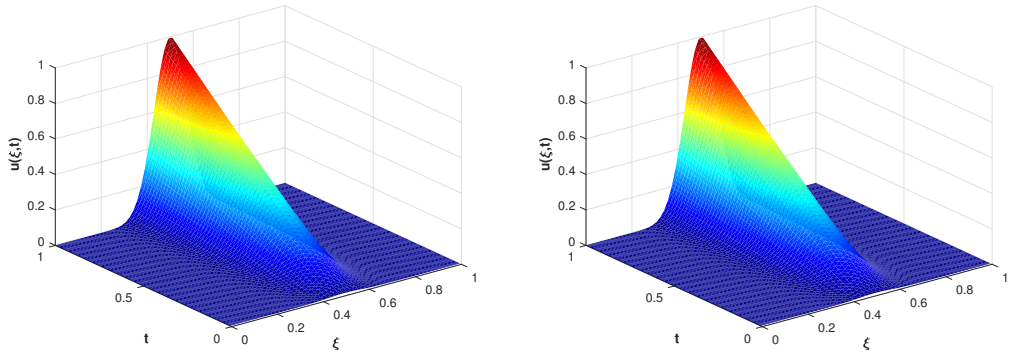

(**a**) (**b**)

Figure 4. (**a**) Approximate solution of Problem 1 using $\alpha = 0.7,\ \gamma = 0.01$. (**b**) Analytic solution of Problem 1 with $\gamma = 0.01, \alpha = 0.7$. It is observed that the numerical solution and exact solutions are in good agreement.

4.2. Problem 2

Here we consider a mobile-immobile advection-dispersion equation of fractional order as [6]

$$D_t u(\xi,t) + D_t^{\alpha} u(\xi,t) = D_{\xi\xi} u(\xi,t) - D_{\xi} u(\xi,t) + f(\xi,t),\ \xi \in [0,1],\ t > 0,$$

where

$$f(\xi,t) = 10\xi^2(1-\xi)^2\left(1 + \frac{t^{1-\alpha}}{\Gamma(2-\alpha)}\right) + 10(t+1)(-2 + 14\xi - 18\xi^2 + 4\xi^3).$$

the analytic solution is given as

$$u(\xi,t) = 10(t+1)\xi^2(1-\xi)^2.$$

This problem is solved using the proposed method with boundary and initial data extracted from the analytic solution. Table 2 shows the results for fractional orders $\alpha = 0.1,\ 0.8$ and various spatial nodes N in the global, and n local domains and quadrature nodes M. From Table 2 we observe that the proposed numerical scheme results with good accuracy. We have compared our results with another RBF method, it can be seen that our results are better. Also, in Table 3 the approximate solution and L_∞ errors obtained via the proposed method are compared with the method in [15], and we see that the results produced by the proposed method are better. The contour plot of absolute error with $N = 75, n = 15, \alpha = 0.8$, and $M = 26$. is shown in Figure 5a. The solution behavior for $t = 0.2,\ 0.4,\ 0.6,\ 0.8,\ 1$ with $N = 60,\ \alpha = 0.7,\ n = 12,\ M = 28$ is shown in Figure 5b. Figure 6a depict the profiles of approximate and analytic solution with $N = 95,\ n = 20, \alpha = 0.8$, at $t = 1$, and absolute error is shown in Figure 6b. The surface plots of the approximate and analytic solutions corresponding to problem 2 with $\alpha = 0.5$ are presented in Figure 7a,b respectively. All the figures and tables demonstrate that the numerical results agree well with the exact solution.

Table 2. The approximate solutions for $10^{12} < \kappa < 10^{16}$, and $\xi \in [0,1]$, and $t = 1$, corresponding to Problem 2.

N	n	M	$\alpha = 0.1$		$\alpha = 0.8$	
			L_∞	$CPU(s)$	L_∞	$CPU(s)$
20	5	26	1.26×10^{-4}	0.179173	1.26×10^{-4}	0.104272
40			4.37×10^{-5}	0.125094	4.44×10^{-5}	0.133066
60			1.34×10^{-5}	0.150076	1.34×10^{-5}	0.132823
70			1.28×10^{-5}	0.210703	1.31×10^{-5}	0.121223
80			1.48×10^{-5}	0.126827	1.51×10^{-5}	0.158628
100			3.28×10^{-6}	0.171984	3.29×10^{-6}	0.141549
75	5	28	1.18×10^{-5}	0.252266	1.20×10^{-5}	0.130174
	7		6.86×10^{-5}	0.191000	6.99×10^{-5}	0.129424
	8		6.31×10^{-5}	0.116571	6.42×10^{-5}	0.142768
	12		3.35×10^{-5}	0.132618	3.37×10^{-5}	0.148221
	16		4.03×10^{-5}	0.146538	4.04×10^{-5}	0.147644
[6]			3.36×10^{-4}		2.96×10^{-4}	

Table 3. The comparison of approximate solutions and L_∞ errors of our method with $n = 5$, $M = 28, 10^{+12} < \kappa < 10^{+16}$ at $t = 1$, and the method in [15] corresponding to Problem 2.

ξ	Exact Solution	Method of [15]		Our Method	
		Approximate Solution	L_∞	Approximate Solution	L_∞
0.10	0.1620	0.1618	1.56×10^{-4}	0.1620	4.35×10^{-5}
0.20	0.5120	0.5105	1.40×10^{-3}	0.5119	1.33×10^{-4}
0.30	0.8820	0.8790	2.97×10^{-3}	0.8818	1.14×10^{-4}
0.40	1.1520	1.1477	4.29×10^{-3}	1.1517	2.66×10^{-4}
0.50	1.2500	1.2450	4.97×10^{-3}	1.2497	2.89×10^{-4}
0.60	1.1520	1.1471	4.80×10^{-3}	1.1517	2.97×10^{-4}
0.70	0.8820	0.8781	3.81×10^{-3}	0.8818	2.39×10^{-4}
0.80	0.5120	0.5097	2.27×10^{-3}	0.5118	1.67×10^{-4}
0.90	0.1620	0.1612	7.20×10^{-4}	0.1619	8.13×10^{-5}

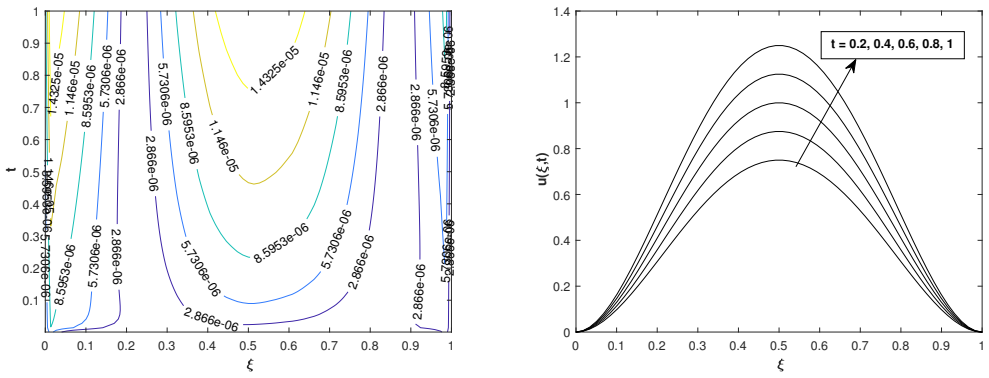

(**a**) (**b**)

Figure 5. (**a**) Contour plot of the absolute error of Problem 2 with $\alpha = 0.8, N = 75, n = 15$, and $M = 26$. (**b**) Solution behavior of Problem 2 at different values of t with $N = 60,\ \alpha = 0.7,\ n = 12,\ M = 28$. It is observed that the solute concentration increases with time.

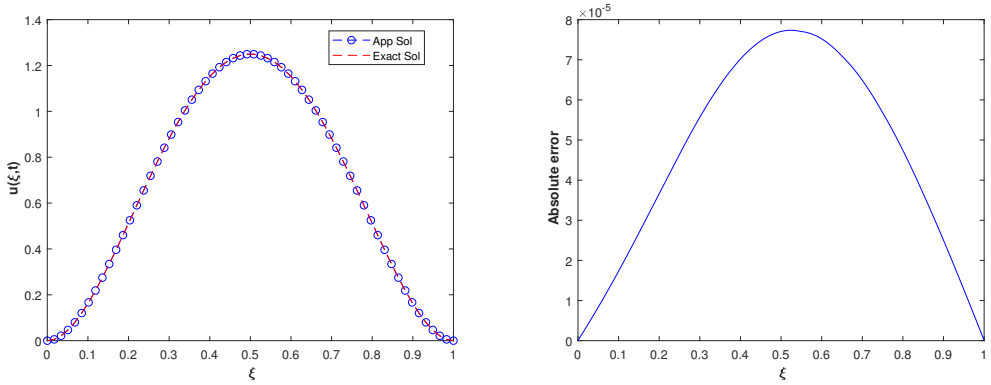

(**a**) (**b**)

Figure 6. (**a**) Plot of approximate solution and exact solutions of Problem 2 with $\alpha = 0.8$. It is seen that the numerical solution agrees well with the exact solution. (**b**) Plot of absolute error of Problem 2 with $\alpha = 0.8, N = 295,\ n = 5,\ M = 28$ at $t = 1$.

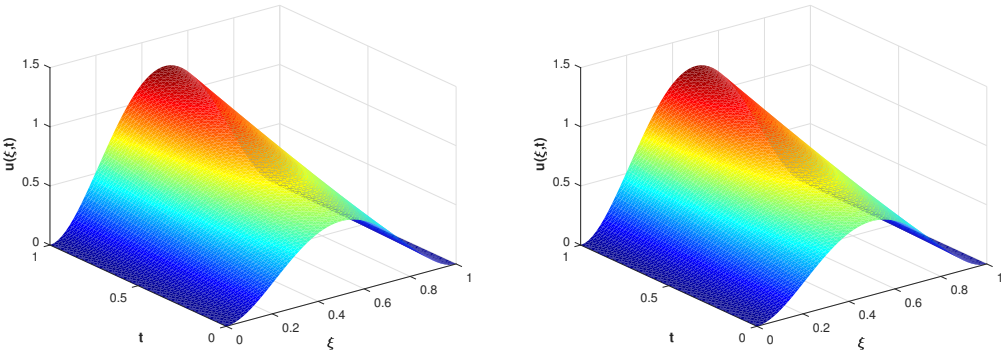

(**a**) (**b**)

Figure 7. (**a**) Approximate solution of Problem 2 with $\alpha = 0.5$. (**b**) Analytic solution of Problem 2 with $\alpha = 0.5$. It is observed that the numerical solution agrees well with the exact solution.

4.3. Problem 3

Here we consider a two-dimensional MI solute transport model

$$D_t u(\xi,\zeta,t) + D_t^{\alpha} u(\xi,\zeta,t) = \Delta u(\xi,\zeta,t) + f(\xi,\zeta,t),\ \xi,\zeta \in [0,1]^2,\ t > 0, \tag{27}$$

where

$$f(\xi,\zeta,t) = \left(2t + 8\pi^2 t^2 + \frac{2t^{2-\alpha}}{\Gamma(3-\alpha)}\right)\cos(2\pi\xi)\cos(2\pi\zeta),$$

and the exact solution is

$$u(\xi,\zeta,t) = t^2\cos(2\pi\xi)\cos(2\pi\zeta).$$

Here we consider a two-dimensional fractional order solute transport model. The problem is solved for $\xi,\zeta \in [0,1]^2$ in regular and regular domains. The boundary and initial conditions are extracted from the analytic solution. The the L_∞ errors obtained for different fractional orders α are depicted in Table 4. In Figure 8a, the regular nodes in the square domain are shown and in Figure 8b the plot of absolute are shown respectively. In Figure 9a,b the analytic and approximate solutions for $t = 0.2 : 0.2 : 1$ are shown. The regular nodes distribution in circular domain and absolute errors are presented in Figure 10a,b respectively. Similarly the regular nodes in nut-shape domain and absolute

error are shown in Figure 11a,b. The obtained results led us to the conclusion that the proposed method performed efficiently in both regular and irregular domains.

Table 4. The L_∞ error for different fractional orders α of problem 3.

M	n	N	$\alpha = 0.25$	$\alpha = 0.5$	$\alpha = 0.75$	$\alpha = 0.85$
26	30	20	1.99×10^{-3}	1.97×10^{-3}	1.96×10^{-3}	1.95×10^{-3}
		22	1.30×10^{-3}	1.29×10^{-3}	1.29×10^{-3}	1.28×10^{-3}
		24	9.67×10^{-4}	9.65×10^{-4}	9.63×10^{-4}	9.63×10^{-3}
		26	7.97×10^{-4}	7.96×10^{-4}	7.95×10^{-4}	7.95×10^{-4}
		28	6.81×10^{-4}	6.79×10^{-4}	6.77×10^{-4}	6.76×10^{-4}
28	26	25	4.61×10^{-3}	4.56×10^{-3}	4.50×10^{-3}	4.48×10^{-3}
	27		4.48×10^{-3}	4.42×10^{-3}	4.37×10^{-3}	4.35×10^{-3}
	28		2.87×10^{-3}	2.83×10^{-3}	2.80×10^{-3}	2.78×10^{-3}
	29		8.38×10^{-4}	8.37×10^{-4}	8.35×10^{-4}	8.35×10^{-4}
	30		8.32×10^{-4}	8.31×10^{-4}	8.30×10^{-4}	8.30×10^{-4}

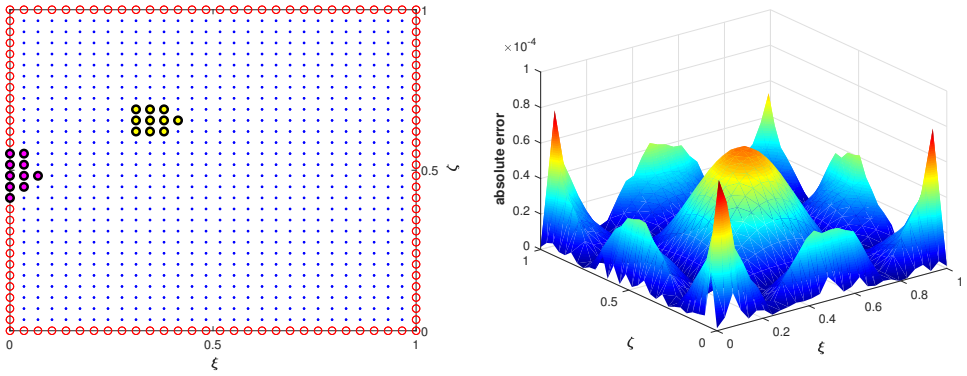

(**a**) (**b**)

Figure 8. (**a**) Square domain with $N = 900$ in the global domain and $n = 20$ in the local domain, magenta corresponds to boundary and yellow corresponds to interior nodes. (**b**) Absolute error of Problem 3 with $\alpha = 0.85$, $N = 900$, $n = 30$, and $M = 28$.

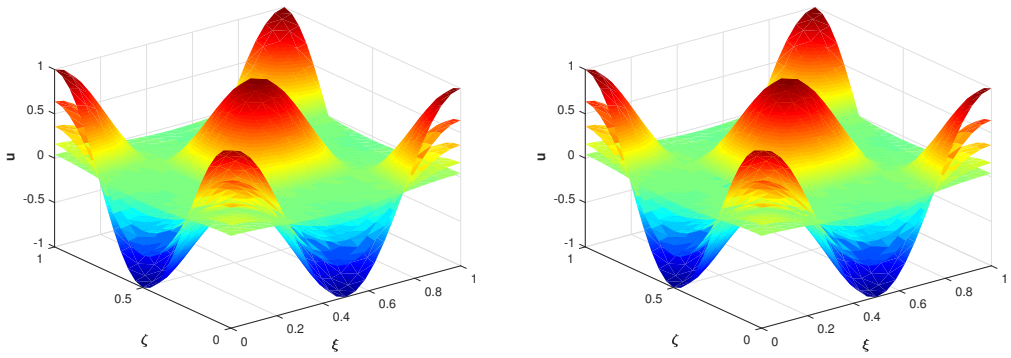

(**a**) (**b**)

Figure 9. (**a**) Analytic solution of Problem 3 with $\alpha = 0.75$, $N = 625$, $n = 30$, and $M = 26$. (**b**) Approximate solution of Problem 3 with $\alpha = 0.75$, $N = 625$, $n = 30$, and $M = 26$. The profiles are plotted for $t = 0.2 : 0.2 : 1$, we see that with an increase in t, the solute concentration increases, and peaks in the profiles have been observed at the center and end points. Similarly, nodes in the profiles have been seen, which show the standing wave behavior of the solution.

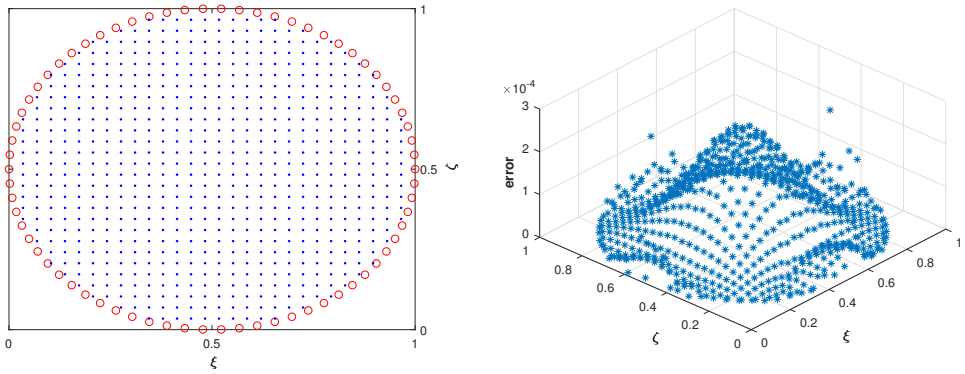

(**a**) (**b**)

Figure 10. (**a**) Circular domain $N = 718$. (**b**) Absolute error corresponding to Problem 3 with $\alpha = 0.25, N = 718, n = 25$, and $M = 26$. It is observed that the proposed scheme has acceptable accuracy.

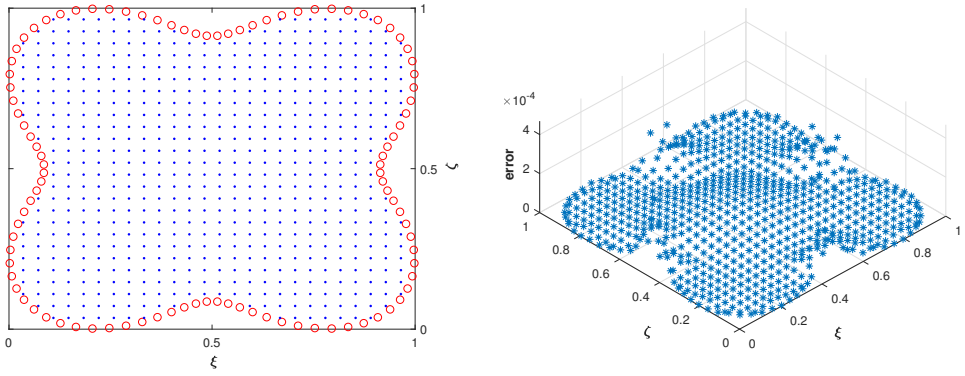

(**a**) (**b**)

Figure 11. (**a**) Nut Shape domain $N = 716$. (**b**) absolute error of Problem 3 with $N = 716, n = 35$, $\alpha = 0.65$, and $M = 26$. It can be seen that the proposed numerical scheme has performed well in the nut shape domain.

4.4. Problem 4

Here we consider a two-dimensional MI solute transport model

$$D_t u(\xi,\zeta,t) + D_t^{\alpha} u(\xi,\zeta,t) = \Delta u(\xi,\zeta,t) + f(\xi,\zeta,t),\ \xi,\zeta \in [0,1]^2,\ t > 0, \tag{28}$$

where

$$f(\xi,\zeta,t) = \left(2t - 2t^2 + \frac{2t^{2-\alpha}}{\Gamma(3-\alpha)}\right) exp(\xi+\zeta),$$

and the analytic solution is

$$u(\xi,\zeta,t) = t^2 e^{(\xi+\zeta)}.$$

Here we consider another two-dimensional fractional order solute transport model. The problem is solved for $\xi,\zeta \in [0,1]^2$ in regular and regular domains. The boundary and initial conditions are extracted from the analytic solution. The Table 5 shows the L_∞ errors obtained for different fractional orders α in the square domain. In Figure 12a the square domain and in Figure 12b the plot of absolute are shown respectively. In Figure 13a,b the analytic and approximate solutions for $t = 0.2 : 0.2 : 1$ are shown. The L-shape domain and absolute errors are presented in Figure 14a,b respectively. Similarly, the star-shape domain and absolute error are shown in Figure 15a,b. The obtained results led us to the conclusion that the proposed method performed efficiently in both regular and irregular domains.

Table 5. The L_∞ error for different fractional orders α of problem 4.

M	n	N	$\alpha = 0.25$	$\alpha = 0.5$	$\alpha = 0.75$	$\alpha = 0.85$
24	30	16	6.83×10^{-4}	6.80×10^{-4}	6.78×10^{-4}	6.77×10^{-4}
		18	7.84×10^{-4}	7.82×10^{-4}	7.79×10^{-4}	7.78×10^{-4}
		20	8.30×10^{-4}	8.28×10^{-4}	8.27×10^{-4}	8.26×10^{-4}
		22	7.82×10^{-4}	7.80×10^{-4}	7.78×10^{-4}	7.77×10^{-4}
		24	7.88×10^{-4}	7.85×10^{-4}	7.81×10^{-4}	7.79×10^{-4}
		26	9.95×10^{-4}	9.87×10^{-4}	9.79×10^{-4}	9.76×10^{-4}
26	25	26	2.86×10^{-3}	2.82×10^{-3}	2.79×10^{-3}	2.77×10^{-3}
	26		2.63×10^{-3}	2.61×10^{-3}	2.58×10^{-3}	2.57×10^{-3}
	27		1.51×10^{-3}	1.50×10^{-3}	1.49×10^{-3}	1.49×10^{-3}
	28		1.03×10^{-3}	1.02×10^{-3}	1.02×10^{-3}	1.01×10^{-3}
	29		9.04×10^{-4}	8.99×10^{-4}	8.93×10^{-4}	8.90×10^{-4}

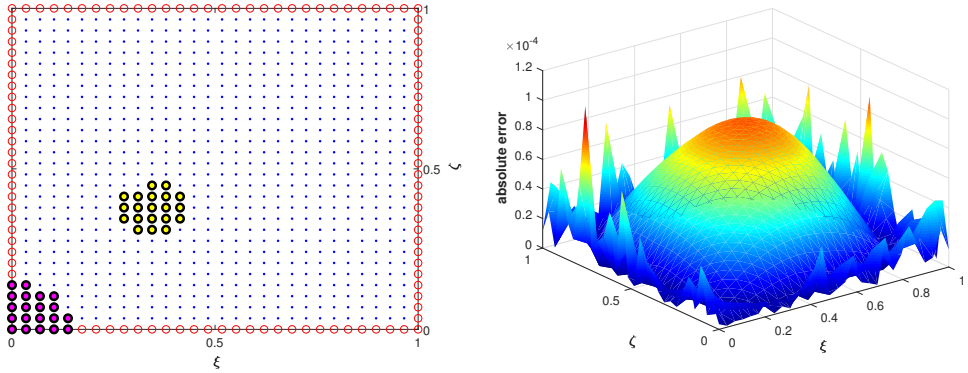

(**a**) (**b**)

Figure 12. (**a**) Square domain with $N = 900$ in global domain and $n = 20$ in local domain, magenta corresponds to boundary and yellow corresponds to interior nodes. (**b**) Absolute error of Problem 4 with $\alpha = 0.85, N = 900, n = 30$, and $M = 28$.

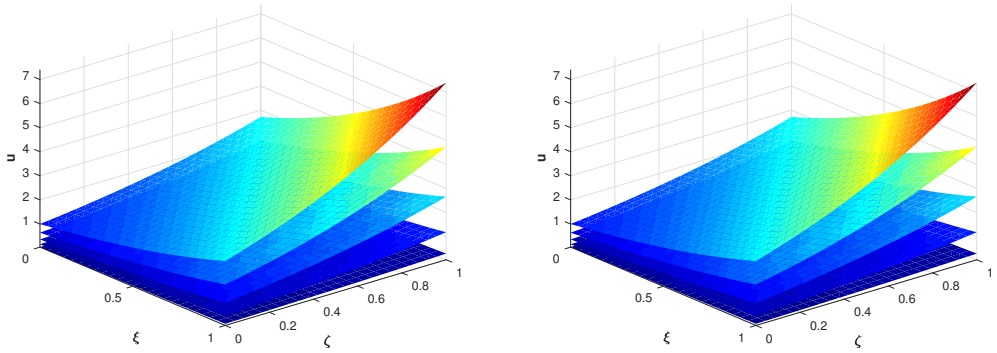

(**a**) (**b**)

Figure 13. (**a**) Analytic solution of Problem 4 with $\alpha = 0.85, N = 625, n = 25$, and $M = 26$. (**b**) Approximate solution of Problem 4 with $\alpha = 0.85, N = 625, n = 25$, and $M = 26$. The numerical solution is in good agreement with the exact solution.

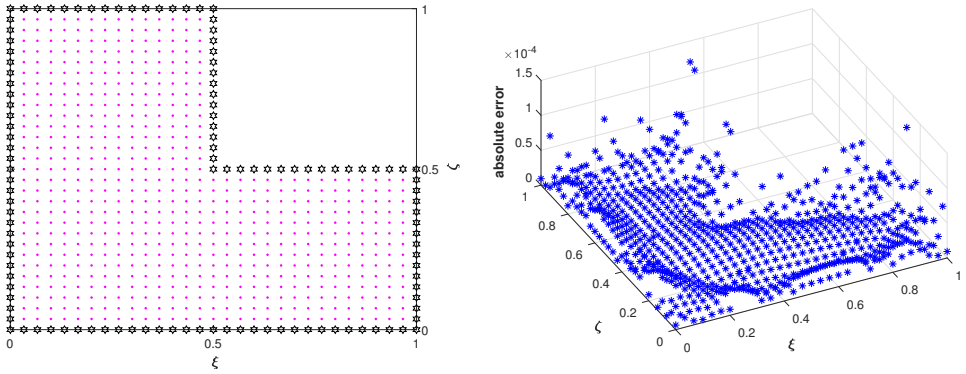

(**a**) (**b**)

Figure 14. (**a**) L Shape domain $n = 20$, $N = 736$. (**b**) Absolute error of Problem 4 with $\alpha = 0.50$, $N = 736, n = 20$, and $M = 26$. In L Shape domain also the method has acceptable accuracy.

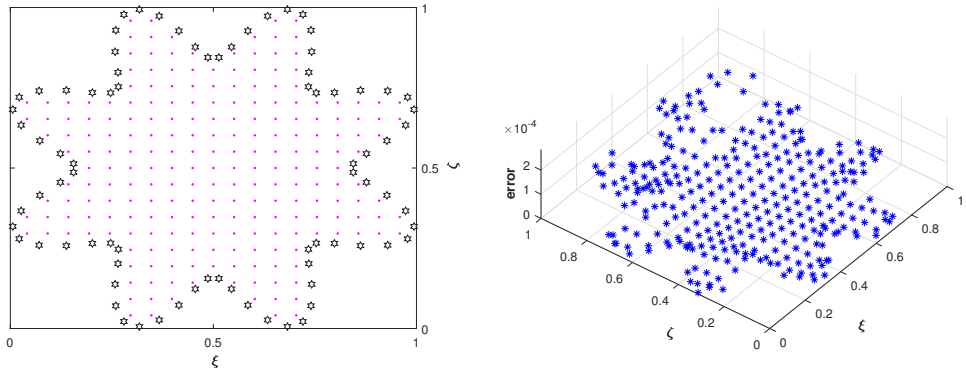

(**a**) (**b**)

Figure 15. (**a**) Star Shape domain $N = 305$. (**b**) absolute error of Problem 4 with $\alpha = 0.75, N = 305$, $n = 30$, and $M = 26$. It can be seen that the method has produced accurate results for a relatively small number of nodes N in the Star shape domain.

5. Conclusions

In this work, we proposed a numerical method for the fractional order MI advection-dispersion models. We transformed the time-fractional derivative via Laplace transform to avoid the classical time stepping method. The local RBF method based on the multiquadric kernels was utilized for the approximation of spatial operators. We discussed the stability and convergence of the proposed numerical scheme. Numerical experiments were performed in one and two dimensions. The local method performed efficiently in irregular domains with acceptable accuracy. The obtained results were compared with other available methods which clearly showed the superiority of the proposed method. Hence we conclude that the present method can solve such problems accurately and efficiently.

Author Contributions: Conceptualization, K., S.K., M.F. and A.A.; Data curation, K. and S.K.; Formal analysis, S.E.A., F.M.A. and A.A.; Funding acquisition, S.E.A. and F.M.A.; Investigation, K., S.K. and A.A.; Supervision, M.F.; Writing—original draft, K. and S.K.; Writing—review & editing, S.E.A. and F.M.A. All authors have read and agreed to the published version of the manuscript.

Funding: The authors would like to thank the Deanship of Scientific Research at Umm Al-Qura University for supporting this work by Grant Code: (22UQU4282396DSR15).

Institutional Review Board Statement: Not applicable.

Informed Consent Statement: Not applicable.

Data Availability Statement: All the data were computed using our algorithm.

Conflicts of Interest: The authors declare no conflict of interest.

References

1. Coats, K.H.; Smith, B.D. Dead-end pore volume and dispersion in porous media. *Soc. Pet. Eng. J.* **1964**, *4*, 73–84. [CrossRef]
2. Chen, Z.; Qian, J.; Zhan, H.; Chen, L.; Luo, S. Mobile-immobile model of solute transport through porous and fractured media. *IAHS-AISH Publ.* **2011**, *341*, 154–158.
3. Bauget, F.; Fourar, M. Non-Fickian dispersion in a single fracture. *J. Contam. Hydrol.* **2008**, *100*, 137–148. [CrossRef] [PubMed]
4. Berkowitz, B. Characterizing flow and transport in fractured geological media: A review. *Adv. Water. Resour.* **2002**, *25*, 861–884. [CrossRef]
5. Benson, D.A.; Schumer, R.; Meerschaert, M.M.; Wheatcraft, S.W. Fractional dispersion, Lévy motion, and the MADE tracer tests. *Transp. Porous. Media.* **2001**, *42*, 211–240. [CrossRef]
6. Golbabai, A.; Nikan, O.; Nikazad, T. Numerical investigation of the time fractional mobile-immobile advection-dispersion model arising from solute transport in porous media. *Int. J. Appl. Comput. Math.* **2019**, *5*, 1–22. [CrossRef]
7. Podlubny, I. An introduction to fractional derivatives, fractional differential equations, to methods of their solution and some of their applications. *Math. Sci. Eng* **1999**, *198*, 340.
8. Diethelm, K.; Ford, N.J. Analysis of fractional differential equations. *J. Math. Anal. Appl.* **2002**, *265*, 229–248. [CrossRef]
9. Mainardi, F.; Carpinteri, A. *Fractals and Fractional Calculus in Continuum Mechanics*; Springer: Berlin/Heidelberg, Germany, 1997.
10. Tarasov, V. E. *Fractional Dynamics: Applications of Fractional Calculus to Dynamics of Particles, Fields and Media*; Springer Science & Business Media: Berlin/Heidelberg, Germany, 2011.
11. Kamran Ali, A.; Gómez-Aguilar, J.F.A transform based local RBF method for 2D linear PDE with Caputo-Fabrizio derivative. *Comptes Rendus. Math.* **2020**, *358*, 831–842. [CrossRef]
12. Kamran; Shah, Z.; Kumam, P.; Alreshidi, N.A. A meshless method based on the Laplace transform for the 2D multi-term time fractional partial integro-differential equation. *Mathematics* **2020**, *8*, 1972. [CrossRef]
13. Schumer, R.; Benson, D.A.; Meerschaert, M.M.; Baeumer, B. Fractal mobile/immobile solute transport. *Water Resour. Res.* **2003**, *39*, 10. [CrossRef]
14. Liu, Q.; Liu, F.; Turner, I.; Anh, V.; Gu, Y. A RBF meshless approach for modeling a fractal mobile/immobile transport model. *Appl. Math. Comput.* **2014**, *226*, 336–347. [CrossRef]
15. Zhang, H.; Liu, F.; Phanikumar, M.S.; Meerschaert, M.M. A novel numerical method for the time variable fractional order mobile-immobile advection-dispersion model. *Comput. Math. Appl.* **2013**, *66*, 693–701. [CrossRef]
16. Liu, F.; Zhuang, P.; Burrage, K. Numerical methods and analysis for a class of fractional advection-dispersion models. *Comput. Math. Appl.* **2012**, *64*, 2990–3007. [CrossRef]
17. Ma, H.; Yang, Y. Jacobi spectral collocation method for the time variable-order fractional mobile-immobile advection-dispersion solute transport model. *East Asian J. Appl. Math.* **2016**, *6*, 337–352. [CrossRef]
18. Jaiswal, S.; Chopra, M.; Das, S. Numerical solution of a space fractional order solute transport system. *J. Porous Media.* **2018**, *21*, 145–160. [CrossRef]
19. Nong, L.; Chen, A. Numerical schemes for the time-fractional mobile/immobile transport equation based on convolution quadrature. *J. Appl. Math. Comput.* **2022**, *68*, 199–215. [CrossRef]
20. Bendjaballah-Lalaoui, N.; Merzougui, A.; Rennane, S. Modeling Solute Transport in Saturated Soil Column: Coupling Physical Nonequilibrium Model and Nonlinear Freundlich Isotherm. *J. Porous Media* **2021**, *24*, 19–35.
21. Sharma, P.K.; Shukla, S.K.; Choudhary, R.; Swami, D. Modeling for solute transport in mobile-immobile soil column experiment. *ISH J. Hydraul. Eng.* **2016**, *22*, 204–211. [CrossRef]
22. Gao, G.; Feng, S.; Zhan, H.; Huang, G.; Mao, X. Evaluation of anomalous solute transport in a large heterogeneous soil column with mobile-immobile model. *J. Hydrol. Eng.* **2009**, *14*, 966–974. [CrossRef]
23. Nikan, O.; Machado, J.T.; Golbabai, A.; Nikazad, T. Numerical approach for modeling fractal mobile/immobile transport model in porous and fractured media. *Int. Commun. Heat Mass Transf.* **2020**, *111*, 104443. [CrossRef]
24. Salomoni, V.A.L.; De Marchi, N. Numerical Solutions of Space-Fractional Advection-Diffusion-Reaction Equations. *Fractal. Fract.* **2022**, *6*, 21. [CrossRef]
25. Belytschko, T.; Lu, Y.Y.; Gu, L. Element-free Galerkin methods. *Int. J. Numer. Methods. Eng.* **1994**, *37*, 229–256. [CrossRef]
26. Fu, Z.; Chen, W.; Zhang, C. Boundary particle method for Cauchy inhomogeneous potential problems. *Inverse Probl. Sci. Eng.* **2012**, *20*, 189–207. [CrossRef]
27. Babuska, I.; Melenk, J. The partition of unity method. *Int. J. Numer. Meth. Engrg.* **1997**, *40*, 727–758. [CrossRef]
28. Sarra, S.A.; Kansa, E.J. Multiquadric radial basis function approximation methods for the numerical solution of partial differential equations. *Adv. Comput. Mech.* **2009**, *2*, 220.
29. Kansa, E.J. Multiquadrics scattered data approximation scheme with applications to computational fluid-dynamics-I, surface approximations and partial derivative estimates. *Comput. Math. Appl.* **1990**, *19*, 127–145. [CrossRef]
30. Sarra, S.A. A local radial basis function method for advection-diffusion-reaction equations on complexly shaped domains. *Appl. Math. Comput.* **2012** , *218*, 9853–9865. [CrossRef]

31. Fasshauer, G.E.; Zhang, J.G. On choosing "optimal" shape parameters for RBF approximation. *Numer. Algorithms* **2007**, *45*, 345–368. [CrossRef]
32. Koupaei, J.A.; Firouznia, M.; Hosseini, S.M.M. Finding a good shape parameter of RBF to solve PDEs based on the particle swarm optimization algorithm. *Alex. Eng. J.* **2018**, *57*, 3641–3652. [CrossRef]
33. Uddin, M. On the selection of a good value of shape parameter in solving time-dependent partial differential equations using RBF approximation method. *Appl. Math. Model.* **2014**, *38*, 135–144. [CrossRef]
34. Šarler, B.; Vertnik, R. Meshfree explicit local radial basis function collocation method for diffusion problems. *Comput. Math. Appl.* **2006**, *51*, 1269–1282. [CrossRef]
35. Yao, G.; Duo, J.; Chen, C.S.; Shen, L.H. Implicit local radial basis function interpolations based on function values. *Appl. Math. Comput.* **2015**, *265*, 91–102. [CrossRef]
36. Divo, E.; Kassab, A.J. An efficient localized RBF meshless method for fluid flow and conjugate heat transfer. *ASME J. Heat. Trans.* **2007**, *129*, 124–136. [CrossRef]
37. Vertnik, R.; Šarler, B. Meshless local radial basis function collocation method for convective-diffusive solid-liquid phase change problems. *Int. J. Numer. Methods. Heat Fluid Flow* **2006**, *16*, 617–640. [CrossRef]
38. Yao, G.; Islam, S.; Šarler, B. Assessment of global and local meshless methods based on collocation with radial basis functions for parabolic partial differential equations in three dimensions. *Eng. Anal. Bound. Elem.* **2012**, *36*, 1640–1648. [CrossRef]
39. Kamran; Ahmadian, A.; Salahshour, S.; Salimi, M. A robust numerical approximation of advection diffusion equations with nonsingular kernel derivative. *Phys. Scr.* **2021**, *96*, 124015. [CrossRef]
40. Davies, A.J.; Crann, D.; Kane, S.J.; Lai, C.H. A hybrid Laplace transform/finite difference boundary element method for diffusion problems. *Comput. Model. Eng. Sci.* **2007**, *18*, 79–86.
41. Fu, Z.J.; Chen, W.; Yang, H.T. Boundary particle method for Laplace transformed time fractional diffusion equations. *J. Comput. Phys.* **2013**, *235*, 52–66. [CrossRef]
42. Rizzo, F.J.; Shippey, D.J. A method of solution of certain problems of transient heat conduction. *AIAA J.* **1970**, *8*, 2004–2009. [CrossRef]
43. Thomée, V. A high order parallel method for time discretization of parabolic type equations based on Laplace transformation and quadrature. *Int. J. Numer. Anal. Model.* **2005**, *2*, 85–96.
44. McLean, W.; Thomée, V. Numerical solution via Laplace transforms of a fractional order evolution equation. *J. Integral Equ. Appl.* **2010**, *22*, 57–94. [CrossRef]
45. López-Fernández, M.; Palencia, C.; Schädle, A. A spectral order method for inverting sectorial Laplace transforms. *SIAM J. Numer. Anal.* **2006**, *44*, 1332–1350. [CrossRef]
46. Kamran; Uddin, M.; Ali, A. On the approximation of time-fractional telegraph equations using localized kernel-based method. *Adv. Differ. Equ.* **2018**, *2018*, 305. [CrossRef]
47. Schaback, R. Error estimates and condition numbers for radial basis function interpolation. *Adv. Comput. Math.* **1995**, *3*, 251–264. [CrossRef]
48. Trefethen, L.N.; Bau, D. *Numerical Linear Algebra*; SIAM: Philadelphia, PA, USA, 1997.
49. Weideman, J.A.C. Optimizing Talbot's contours for the inversion of the Laplace transform. *SIAM J. Numer. Anal.* **2006**, *44*, 2342–2362. [CrossRef]
50. Talbot, A. The accurate numerical inversion of Laplace transforms. *IMA J. Appl. Math.* **1979**, *23*, 97–120. [CrossRef]
51. Martensen, E. Zur numerischen auswertung uneigentlicher integrale. *Z. Angew. Math. Mech* **1968**, *48*, T83–T85.
52. Dingfelder, B.; Weideman, J.A.C. An improved Talbot method for numerical Laplace transform inversion. *Numer. Algorithms* **2015**, *68*, 167–183. [CrossRef]